NEURAL-NETWORK-BASED PLASMA-ACTUATED FLOW SEPARATION CONTROL IN A SUDDENLY EXPANDED DUCT: AN EDDY-RESOLVING RANS MODELING

Tarik Čorbo, Suad Jakirlić
Institute of Fluid Mechanics and Aerodynamics, Technical University of Darmstadt,
Peter-Grünberg-Str. 10, 64287 Darmstadt, Germany
corbo@sla.tu-darmstadt.de, jakirlic@sla.tu-darmstadt.de

ABSTRACT

Flow separation control in a confined backward-facing step configuration at a Reynolds number of $Re = 7100$, based on the hydraulic diameter of the inflow duct and the corresponding bulk velocity, has been computationally investigated using the eddy-resolving version of the conventional $\zeta{-}f$ RANS turbulence model (Hanjalić *et al.* (2004)) as formulated by Krumbein (2018). Preliminary model validation was performed by simulating the baseline case without flow control against the experimental and DNS reference data of Zajec (2021). In order to manipulate the flow with the goal of reducing the separation zone size, a spanwise-oriented dielectric barrier discharge (DBD) plasma actuator was installed on the bottom step wall of the inlet duct. The actuator generates a streamwise-oriented mean vorticity with spanwise flow directed toward the side duct walls, thereby modifying appropriately the secondary flow structures. The adequately restructured secondary flow pattern within the inflow duct aligns with the reorientation of the underlying secondary motion and the associated turbulence. Two models representing the plasma actuator force were employed. The first is based on the time-averaged force measured by Kriegseis (2013), interpolated onto the numerical mesh using a neural network. The second represents the unsteady plasma actuator force, generated from a neural network trained on the data of Kuhnhenn (2016) and further refined with the averaged data from Kriegseis (2013), as described in Corbo & Jakirlic (2026). Particular attention is given to the advantages of the unsteady force representation compared to the steady one, especially regarding its effect on flow reattachment prediction. Large-scale turbulence is simulated with a hybrid, grid-spacing-independent turbulence model formulation, while the unresolved turbulence is described by a near-wall, elliptic-relaxation-based eddy-viscosity RANS model, extended to enable triggering into its fluctuating-mode capacity.

INTRODUCTION

The backward-facing step, which features a fixed separation location that coincides with the step edge, is a suitable configuration for analyzing separated flows, which are relevant to many industrial and engineering applications. In the case of the confined backward-facing step flow geometry, the side duct walls cause a three-dimensional (3D) recirculating flow to form past the step. The flow pattern across the cross-section within the inflow duct resembles Prandtl's secondary flow of the second kind, which is induced by turbulence anisotropy. The use of plasma actuators for flow separation control has been tested numerically by Maden (2015), who used the presently adapted plasma actuator arrangement in a 3D diffuser configuration. They reported that significant changes to the separated flow structure can be achieved by manipulating the secondary flow pattern in the inflow duct. Accordingly, the goal of this study is to examine the effect of this particular plasma actuator on the confined backward-facing step geometry. The plasma actuator will create a pair of streamwise vortices within the inlet duct that rotate in the opposite direction of the vortices formed in the baseline, uncontrolled case.

Additionally, the study focuses on validating the unsteady plasma actuator force model that was originally developed by Corbo & Jakirlic (2026) and subsequently modified. The new model will undergo a comparative assessment against the steady force approach previously used in Maden (2013). The modification is that the plasma actuator force will be interpolated using a neural network. Cases involving plasma-actuated flow and the baseline configuration will be simulated using an eddy-resolving Reynolds-averaged Navier-Stokes (RANS)-based turbulence model.

COMPUTATIONAL METHOD

The cases studied in this work were simulated using OpenFOAM, an open-source, finite-volume C++ library in which all plasma actuator force and turbulence models were implemented. Second-order accuracy is ensured with respect to spatial and temporal discretization. All simulations used a varying time step with the constraint $CFL < 0.7$, and incompressible flow was assumed.

The steady plasma actuator force is obtained as the output of a multilayer perceptron with six hidden layers. This perceptron takes the coordinates of the given cell as input and outputs the force value, which is then used in the momentum equation. This neural network has been trained to predict the force distribution, as measured by Kriegseis (2013). As was done previously, a multilayer perceptron with six hidden layers is also used for the unsteady plasma actuator force. However, this model considers not only the coordinates of the cell point, but also the current simulation time. It then outputs the appropriate force for the given cell coordinates and time. This force is used in the momentum equation as a volume force. This model was trained using unsteady plasma actuator force measurements from Kuhnhenn (2016), along with additional linearly interpolated force fields. However, these measurements alone are insufficient to accurately capture the average force, so average force measurements were also implemented in the training through the loss function:

$$\text{LOSS} = (1-\alpha\Delta)\,\text{RMS}(f_{\text{pred}}, f_{\text{exp}}^{\text{tv}}) + \alpha\Delta\,\text{RMS}(f_{\text{pred}}, f_{\text{exp}}^{\text{avg}}) \quad (1)$$

where Δ represents the difference between the measured average plasma actuator force and the average of the neural network plasma actuator force, and α is a factor between 0 and 1 and determines the influence of the averaged training data and time-varying data. This training procedure is conducted twice. First, $\alpha = 1$ is used, and Δ is obtained from a neural network that is trained only on time-varying measurements. The resulting neural network is then used to obtain new values of Δ, and the optimal value of α is determined to be 0.75. This final neural network is used in the work. The experimental values of the time-varying force are denoted by $f_{\text{exp}}^{\text{tv}}$, the experimental average force by $f_{\text{exp}}^{\text{avg}}$, and the predicted force by f_{pred}.

The RANS turbulence model proposal, sensitized presently to an eddy-resolving model, is based on the elliptic-relaxation eddy viscosity model formulation by Hanjalić *et al.* (2004). As with the original model, the same formulation is used for the equations governing the turbulent kinetic energy (k), normal-to-wall turbulence intensity ($\zeta = \overline{v^2}/k$) and the elliptic-relaxation function (f). To enable the model's capacity to resolve turbulence fluctuations, in accordance with the Scale-Adaptive Simulation (SAS) methodology as introduced by Menter & Egorov (2010), the equation for the viscous dissipation rate (ε) of k is transformed into an equation for the specific dissipation rate, ω, which represents the inverse of the turbulent timescale. This is achieved by applying differentiation rules to the relation, $\omega = \varepsilon/k$. Finally, the RANS-like transport equation for the ω quantity is extended to include an SAS-related production term, modeled in terms of the second derivative of the underlying velocity field $\nabla^2\mathbf{U}$, enabling it to be triggered into resolving mode:

$$\frac{D\omega}{Dt} = \left(\frac{D\omega}{Dt}\right)_{\text{RANS}} + P_{\text{SAS}} \quad (2)$$

The solution domain (Fig. 1) is meshed using the ANSA preprocessing software. The mesh consists of 2.5 million cells, including those of the precursor simulation of the inflow, which runs in parallel and from which the inlet conditions for the main geometry are mapped. The near-wall grid resolution, which copes with integrating the flow-governing equations to the wall, is ensured by situating the first cell deep in the viscous sublayer, with $y^+ \leq 1$. Fig. 1 shows the flow domain geometry with all the necessary dimensions, as well as the plasma actuator arrangement mounted on the lower inflow duct wall immediately before the sharp edge, following the geometry in Zajec (2021). Fig. 2 shows the velocity vectors in the $y-z$ cross-sectional plane of the inflow duct. The left image relates to the baseline uncontrolled case, and the right image shows the field of the averaged unsteady force of the plasma actuator, including the reoriented secondary flow vectors. The plasma actuator is configured such that the force acts contrary to the rotational orientation of the baseline vortices.

RESULTS

Considering that the use of the plasma actuator was done in a numerical experiment capacity, it is necessary to first validate the mesh and model for this case. This is done by comparing the baseline case with the numerical and experimental results at different x locations, where $x = 0$ mm is the location of the step, from Zajec (2021) in Fig. 4. In this figure, the velocity and turbulent kinetic energy profiles are compared for all simulations at four different locations, both inside the inlet channel and after the step, and show good agreement especially for the velocity profiles. The velocity profiles at $x = -10$ mm and $x = 0$ mm show a slight underprediction for the middle of the channel. This is also the case for the turbulent kinetic energy, but crucially the near-wall energy peaks are captured well. At these locations there is no noticeable difference between the baseline case and the actuated cases. At the other two locations further downstream it is clear that the baseline simulation follows the experimental profiles very well, and here a difference between the actuated and baseline cases is clearly visible, where the negative velocity is smaller in the case of the actuated cases. The turbulent kinetic energy profiles at $x = 40$ mm have a slight overprediction in all three simulations and all three are very similar, at $x = 120$ mm the prediction of the baseline case is much closer and here the effect of the plasma actuator is visible where more energy is present at the lower wall. The location at $x = 200$ mm, which is right after the reattachment zone for the baseline case, also shows good agreement for both velocity and turbulent kinetic energy profiles and also showcases the fact that the plasma actuator causes a faster reattachment. These profiles confirm that the mesh and models used are adequate to accurately capture the flow phenomena and also show the effect of the plasma actuator on the flow reattachment.

This effect is highlighted even better in Fig. 5 where the velocity magnitude is shown in conjunction with the streamlines. The actuated cases show a reattachment occurring at approximately 6 step heights, a significant improvement compared to the baseline case where the reattachment is observed at around 8 step heights, which is in agreement with the findings from Zajec (2021) showing that the global flow is captured well in the baseline case. This is a result of the vortices that are induced by the plasma actuator, which are shown in Fig. 2 and impart downward momentum to the main flow, allowing for faster reattachment. Naturally, these vortices are not present in the baseline case, and in Fig. 2 for this case it is clear that the secondary vortices that are a result of the geometry-induced anisotropy are much smaller in intensity and also have a different rotation direction. The plasma actuator not only increases the velocity in the z direction but also forces the main flow down to the bottom wall. This effect is nearly identical for both the steady and unsteady force model. Both the profiles from Fig. 4 and the streamlines from Fig. 5 show that the two different plasma actuator representations do not diverge significantly, if at all. In Fig. 7, the differences between the three simulations are illustrated in terms of profiles at different locations. The top of the figure shows the velocity profiles at different locations and the velocity field for the simulation using the unsteady plasma actuator force. From these profiles it is clear that the influence of the plasma actuator is negligible in the inlet duct and only becomes apparent after the step and only becomes more significant further downstream. Crucially, the faster reattachment caused by the plasma actuator is clear here as well. In the middle and bottom of Fig. 7 the turbulent kinetic energy profiles for all the simulations and the turbulent kinetic energy field for the simulation that uses the unsteady plasma actuator force are shown, and the shear stress profiles for all three simulations and the shear stress field for the simulation using the unsteady plasma actuator model are shown respectively. The turbulent kinetic energy profiles only start showing the influence of the plasma actuator at the locations after two step heights and a tendency to lower the profile peak toward the bottom wall is observed, which is consistent with the faster reattachment. The wall shear stress profiles show a much lower sensitivity to the plasma actuator. The profiles for all three simulations are very similar and start diverging only after 4 step heights. Crucially, all the profiles for the two actuated simulations are nearly identical, showing that there is no significant impact stemming from the force unsteadiness on flow quantities.

Considering this, and in order to further compare the two force models, it is interesting to look at the inlet duct cross section where the plasma actuator is active. Firstly, the turbulent kinetic energy field for all three simulations is shown in Fig. 3 at the location one step height from the step, $x = -25$ mm. The left-most picture represents the baseline case, and clearly the energy is concentrated at the walls. The middle field corresponds to the unsteady plasma actuator force, and here a clear difference from the baseline case is observable at the bottom wall where the plasma actuator acts. In the acceleration zone there is a decrease in turbulence, however right after there is an increase in turbulent kinetic energy, and a high-energy zone that extends further from the wall. This corresponds to the vortex generated by the plasma actuator. A nearly identical field is obtained with the steady force actuation. To get further quantitative insights, profiles are drawn both parallel to the wall (top) at different y locations and perpendicular to the wall (bottom) at different z locations, Fig. 6. Interestingly, the profiles at $y = 10$ mm and $y = 19$ mm, so in the middle of the flow and close to the top wall respectively, show that the influence of the plasma actuator this far away from the bottom wall is negligible, the effect is only observable close to the bottom wall at $y = 1$ mm. This profile, similarly to Fig. 3, shows an increase in turbulence after the acceleration zone, however once again there are no significant differences between the steady and unsteady forces. In the acceleration zone the profiles obtained for the simulation using steady forcing dominate very slightly, however the peak is slightly more pronounced in the simulation using the unsteady plasma actuator force. After the peak it can be seen that the simulation with the unsteady plasma actuator force is ever so slightly more energetic. The wall-normal profiles at $z = 0$ mm and $z = 20$ mm, so in the middle of the channel and close to the side wall respectively, again show that there is no noticeable influence of the plasma actuator. The influence is only visible at $z = 12.5$ mm. Here the profiles are again very similar with the steady force profile showing slightly more energy. This location is also shown to give more energy in the previously discussed profile at $y = 1$ mm, as it is right before the energy peak.

CONCLUSION

In this work the confined backward-facing step flow configuration was simulated using the eddy-resolving $\zeta - f$ model. Flow control was achieved with a dielectric barrier discharge plasma actuator modeled as a volume force in the momentum equation. Two approaches were used to model this force: one that uses the steady plasma actuator force and one that uses a novel unsteady force model, which predicts force values using a neural network. This work has shown the adaptability of the previously used neural network force model to yet another case. The same neural network that was trained and validated to predict the unsteady plasma actuator force from the flat plate case in quiescent air has been adapted to the confined backward-facing step case. This required no additional training or neural network modifications, only slight modifications to the OpenFOAM solver, highlighting the versatility of this approach on different meshes and geometries. Additionally, a neural network has also been trained to predict the steady plasma actuator force in order to simplify the case setup for the simulation that used the steady plasma actuator force. The velocity and turbulent kinetic energy fields for the baseline case showed good agreement with the reference experimental and numerical reference data from Zajec (2021), showing the validity of the mesh and turbulence model for this case. Mean velocity fields showed a significant reduction in the recirculation zone when the plasma actuator was used, with similar results for both models. This reduction in the recirculation zone was attributed to the downward momentum imparted to the main flow by the plasma actuator stemming from the secondary vortices that are created by it. In order to further analyze the differences between the two plasma actuator force models, the inflow duct flow, where the plasma actuator acts, was analyzed. This included both cross-sectional turbulent kinetic energy fields, which showed an increase in turbulence right after the main acceleration zone in the actuated cases not present in the baseline case, but showed no significant differences between the two force models. No significant differences were observed in the wall-parallel and wall-normal profiles in the inflow duct for the two force models. While this case showed no advantage or significant difference in either the velocity or turbulence obtained when using either a steady or unsteady plasma actuator force model, it did highlight the practicality of the neural-network-based force modeling approach and its adaptability to different cases and meshes, not offered by standard interpolation approaches. This work also further validated the eddy-resolving $\zeta - f$ model on yet another highly complex case, highlighting its computational cost-effectiveness.

Acknowledgment. The financial support of the German Academic Exchange Service (DAAD) for T. Čorbo within the framework of the funding program 'Forschungsstipendien - Promotionen in Deutschland (ID 57588370)' is gratefully acknowledged.

REFERENCES

Corbo, T. & Jakirlic, S. 2026 Computational study of a turbulent wall jet induced by a transient plasma actuator force. In *Notes on Numerical Fluid Mechanics and Multidisciplinary Design*, , vol. 156, pp. 601–610. Springer.

Hanjalić, K., Popovac, M. & Hadžiabdic, M. 2004 A robust near-wall elliptic-relaxation eddy-viscosity turbulence model for CFD. *Int. J. Heat and Fluid Flow* **25** (6), 1047–1051.

Kriegseis, J. *et al.* 2013 Velocity-information-based force-term estimation of dielectric-barrier discharge plasma actuators. *Journal of Physics D: Applied Physics* **46** (5), 055202.

Krumbein, B. *et al.* 2018 A scale-resolving elliptic-relaxation-based eddy-viscosity model: development and validation. In *Notes on Numerical Fluid Mechanics and Multidisciplinary Design*, , vol. 142, pp. 90–100. Springer.

Kuhnhenn, M. *et al.* 2016 Interrelation of phase-averaged volume force and capacitance of dielectric barrier discharge plasma actuators. *Journal of Fluid Mechanics* **809**, R1.

Maden, I. *et al.* 2013 Experimental and computational study of the flow induced by a plasma actuator. *Int. J. Heat and Fluid Flow* **41**, 80–89.

Maden, I. *et al.* 2015 Plasma-actuated manipulation of secondary flow towards pressure recovery enhancement in a 3D diffuser modelled by an eddy-resolving second-moment closure. *Flow, Turbulence and Combustion* **95** (2), 377–398.

Menter, F. R. & Egorov, Y. 2010 The scale-adaptive simulation method for unsteady turbulent flow predictions. part 1: theory and model description. *Flow, Turbulence and Combustion* **85** (1), 113–138.

Zajec, B. *et al.* 2021 Turbulent flow over confined backward-facing step: PIV vs. DNS. *Applied Sciences* **11** (22), 10582.

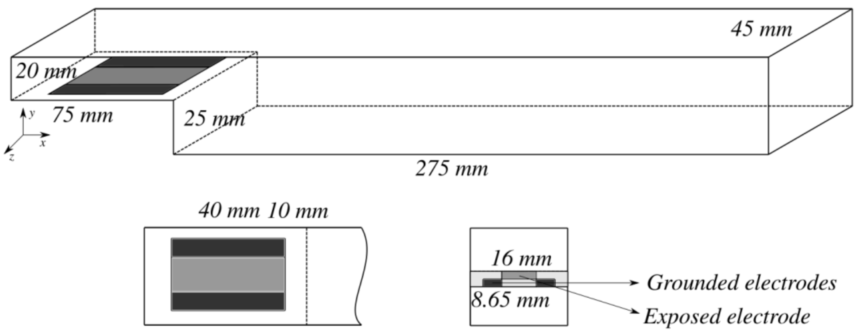

Figure 1. Flow domain geometry and plasma actuator configuration.

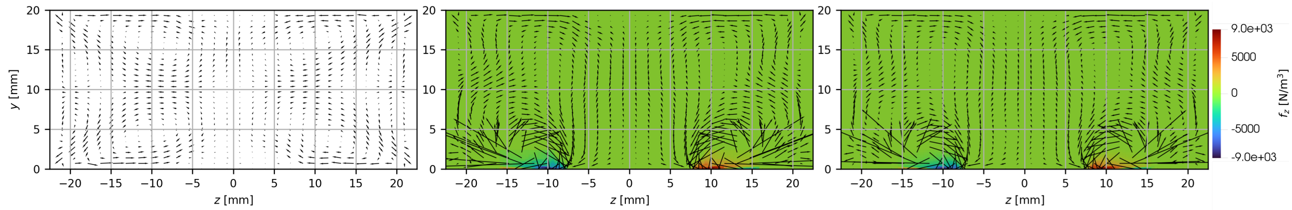

Figure 2. Velocity vectors in the $y-z$ plane for the baseline case (left), the averaged unsteady plasma actuator force field with velocity vectors (middle) and the steady plasma actuator force field with velocity vectors (right).

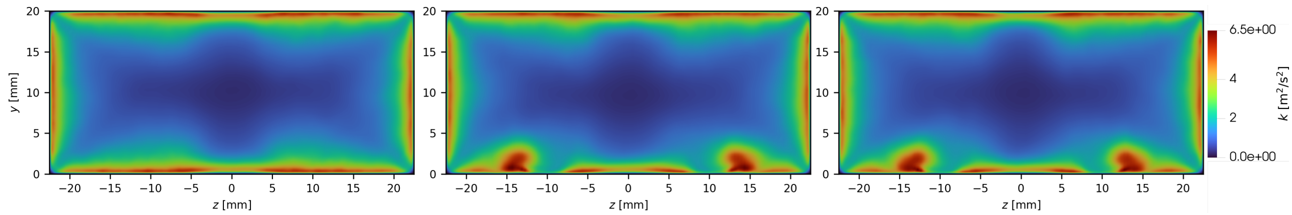

Figure 3. Turbulent kinetic energy fields at the location $x = -25$ mm (one step height before the step) corresponding to the baseline case (left), case with the unsteady plasma actuator force (middle) and case with the steady plasma actuator case (left).

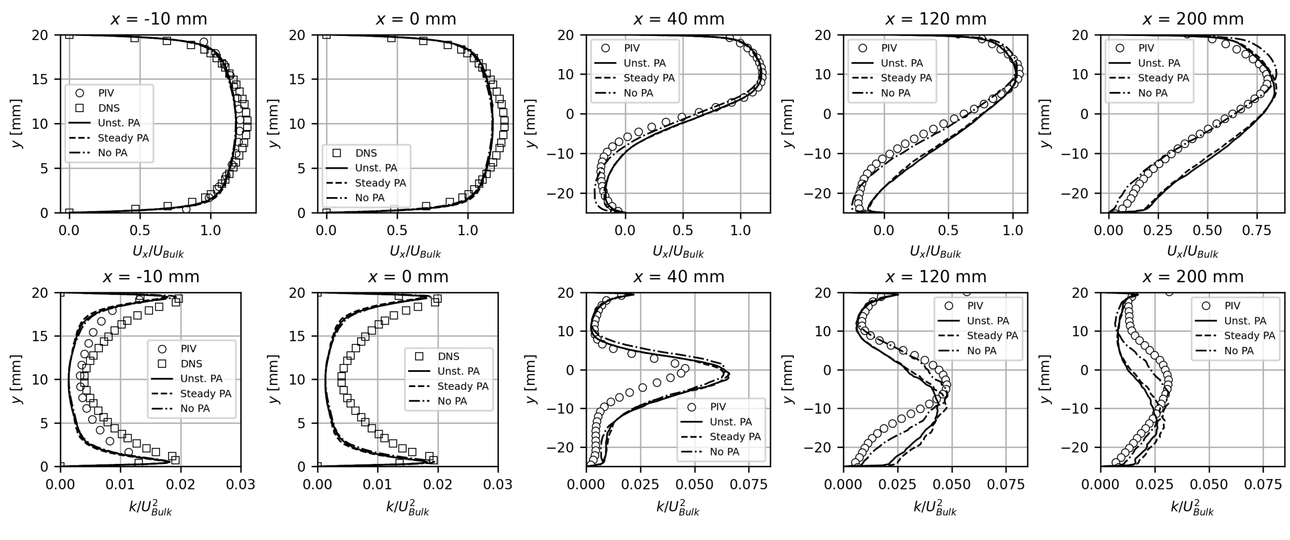

Figure 4. Velocity profiles of all three simulations in different locations in the flow (top) and turbulent kinetic energy profiles for all three simulations at different locations in the flow (bottom).

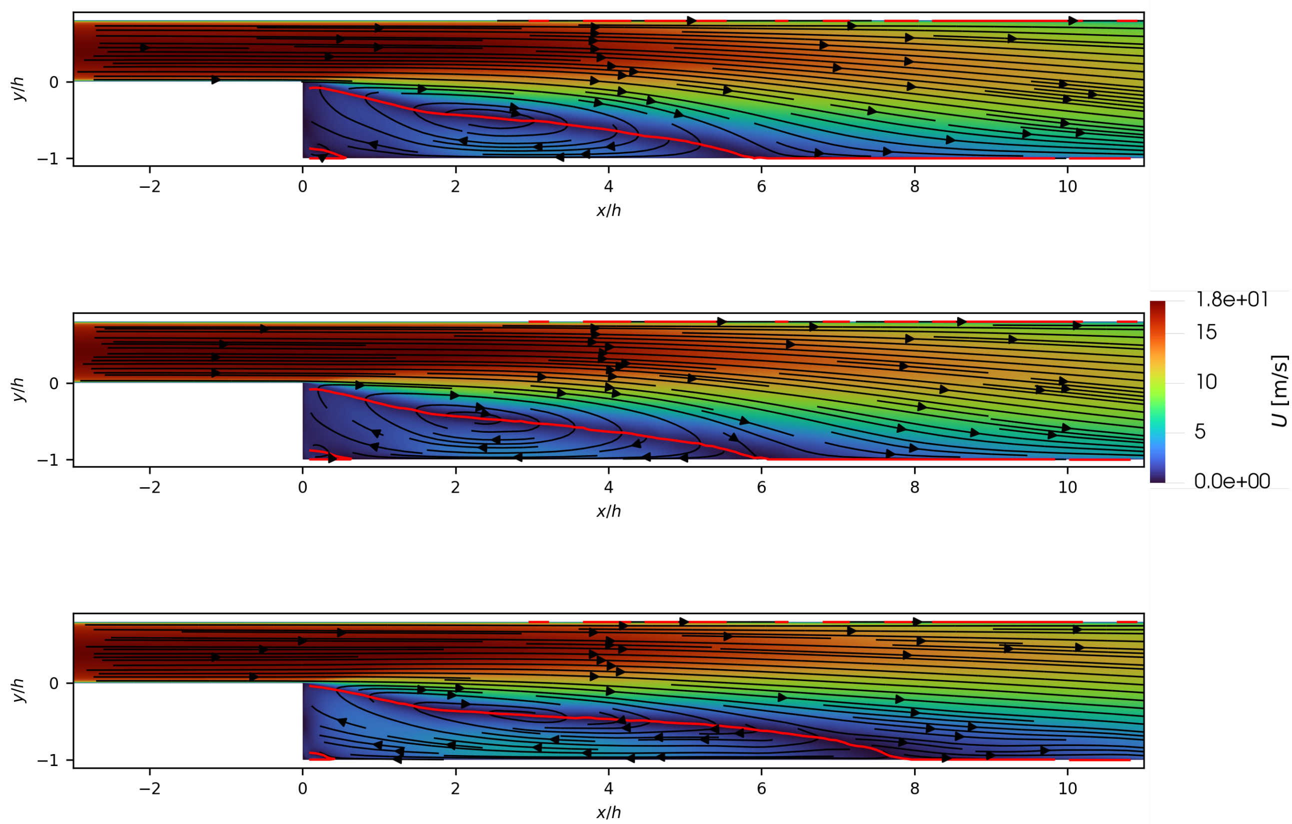

Figure 5. Time-averaged mean streamwise velocity fields and the corresponding streamlines for the controlled cases with an unsteady plasma actuator force (top), a steady plasma actuator force (middle), and the uncontrolled baseline case (bottom).

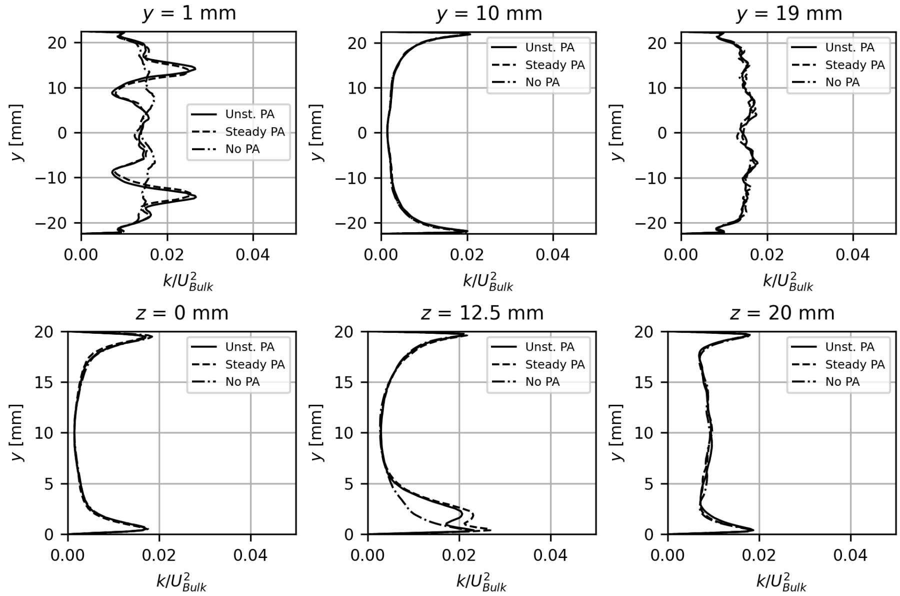

Figure 6. Turbulent kinetic energy profiles in the inlet duct at $x = -25$ mm at different locations parallel to the wall (top) and at different locations perpendicular to the wall (bottom).

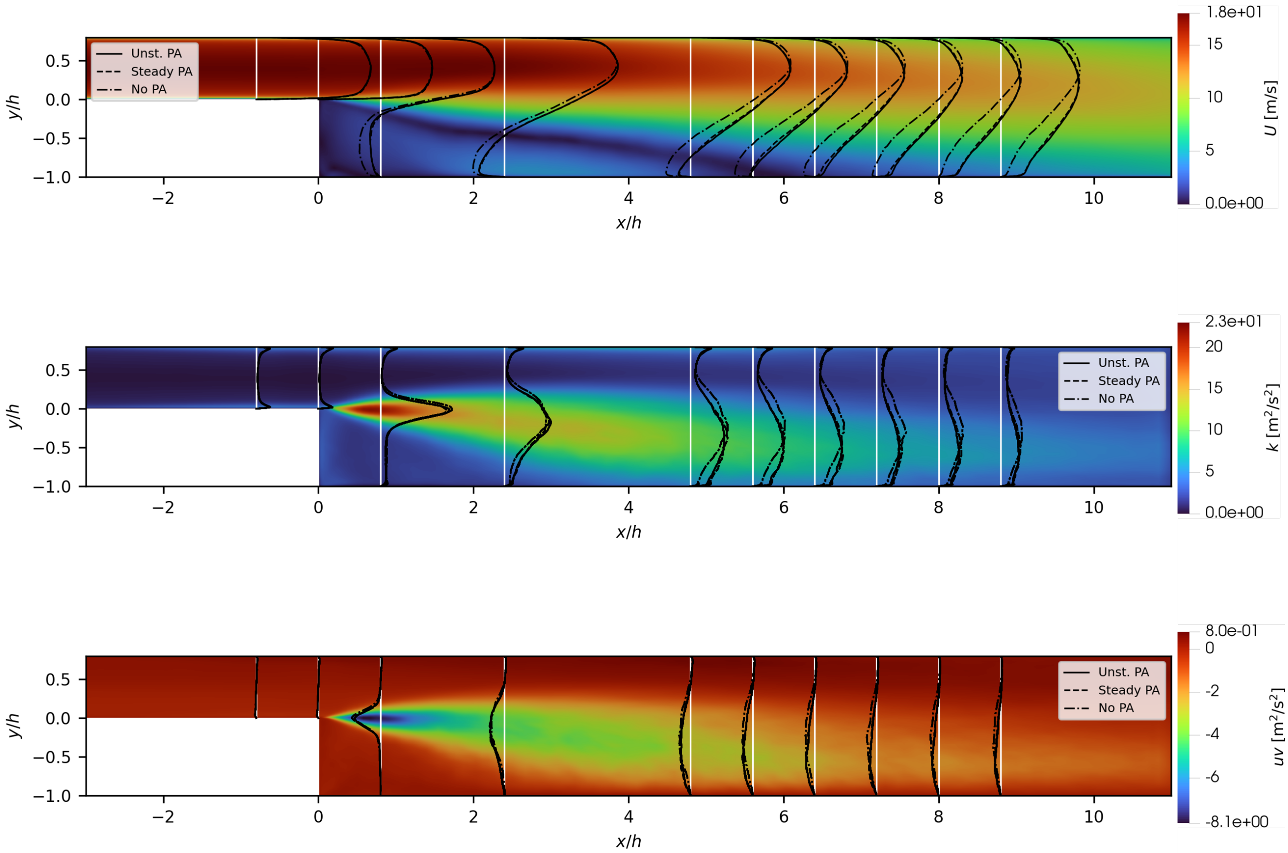

Figure 7. Mean streamwise velocity (top), turbulent kinetic velocity (middle) and shear stress component (bottom) fields from the simulation with the unsteady plasma actuator force with profiles for all three simulations in the middle of the geometry.